Origin Analysis and Mitigation Method of Voltage Oscillation Occurred Inside the Winding of Medium-Voltage Medium-Frequency Transformer

Yueyin Wang, Wu Chen, *Senior Member, IEEE*, Zhan Shen, *Member, IEEE*, Xiao Yu, Xuhao Zhu, Haozhe Jin, *Graduate Student Member, IEEE*, Siyi Luo, *Graduate Student Member, IEEE*, Zewei Hao, and Xin Li, *Member, IEEE*

***Abstract*—The medium-voltage medium-frequency transformer is a critical component of high-power dc converters. However, the ultrafast switching speed of wide bandgap semiconductors can induce voltage oscillations in the medium-frequency transformer, increasing the risk of primary-insulation partial discharge and leading to permanent breakdown. Existing research has focused on voltage oscillations occurring at ports, but there is insufficient knowledge about those happening within the winding. This article presents a model for calculating internal voltage oscillations. Compared to conventional models, it is simple and considers the core electrical energy for the first time. Accordingly, the physically-based analytical formulas are derived to calculate voltage oscillations. Based on the model, the relationship between voltage oscillations, port voltage, and transformer structure is analyzed. The oscillation mitigation method is presented and validated by experiment.**

***Index Terms*—Analytical model, high-frequency oscillation, high-frequency transformer.**

I. Introduction

MEDIUM voltage dc (MVdc) collection grids are adopted in renewable energy systems to increase power density [1], [2], [3]. MVdc converters play a key role in these grids, with the medium-frequency transformer (MFT) as the essential component for providing critical galvanic isolation.

However, the MFTs installed in medium voltage (MV) collection systems encounter severe voltage stresses, which withstand voltage waveforms characterized by high frequencies and rapid slew rates [4], [5], [6]. It can degrade dielectric performance, resulting in partial discharge, increased dielectric losses, aging, and even breakdown [7], [8], [9], [10], [11], [12], [13], [14], [15]. Given the substantial operational costs of typical renewable energy systems such as offshore wind farms and photovoltaic plants, the reliability of high-frequency transformers is highly required. Therefore, it is essential to comprehensively study the voltage stress endured by MFTs in MV systems.

The insulation of MFTs typically has to withstand the highest voltage, and the margin for insulation design is relatively low within the limited space. The repetitive square waves output by converters contain rich harmonics, which form continuous high-frequency voltage oscillations (HFVO). It can lead to MFTs experiencing unexpected voltage stresses over the rated dielectric strength, causing more intense partial discharges, reduced insulation life, and even breakdowns, thus posing a threat to insulation reliability. A rational insulation design is a precondition for maximizing efficiency and power density in the limited space available. Therefore, it is essential to accurately determine the voltage distribution in transformers exposed to HFVO and develop versatile and practical methods to mitigate HFVO.

The primary methods to study HFVO include the finite element method (FEM) and lumped circuit models. The FEM models used for power electronics are often simplified. It means that Maxwell's equations are reduced into a quasi-static model, which includes electrostatic and magnet-static forms depending on their interested situation [16], [17], [18], [19]. It requires significant computational resources and is inefficient for calculating resonances occurring within MFTs.

The lumped circuit model is a promising method for modeling magnetic components. Currently, there are two main approaches, including methods based on measurement data or physical structure. The measurement-based approach includes approximating measured data to the equivalent circuit response via mathematical fitting. It can be achieved through parameter adjustments of a fixed circuit [20], [21] or generating a suitable circuit directly [22], [23]. The approach is accurate within the operating frequency and suitable for black-box texting. However,

Received 12 March 2024; revised 29 May 2024 and 27 July 2024; accepted 6 September 2024. Date of publication 19 September 2024; date of current version 12 December 2024. This work was supported by the National Key R&D Program of China under Grant 2023YFB4204702. Recommended for publication by Associate Editor N. Prabhu. *(Corresponding authors: Wu Chen; Xin Li.)*

Yueyin Wang, Wu Chen, Zhan Shen, Xuhao Zhu, Haozhe Jin, Siyi Luo, Zewei Hao, and Xin Li are with the Center for Advanced Power Conversion Technology and Equipment, School of Electrical Engineering, Southeast University, Nanjing 210096, China (e-mail: yywangee@seu.edu.cn; chenwu@seu.edu.cn; zhs@seu.edu.cn; 230238799@seu.edu.cn; hzjin@seu.edu.cn; siyluo@seu.edu.cn; haozewei@whu.edu.cn; li-xin@seu.edu.cn).

Xiao Yu is with the China Academy of Engineering Physics, Mianyang 621000, China (e-mail: yuxiao@cqu.edu.cn).

Color versions of one or more figures in this article are available at https://doi.org/10.1109/TPEL.2024.3462413.

Digital Object Identifier 10.1109/TPEL.2024.3462413

it lacks a clear physical meaning and is unsuitable for optimizing the design of magnetic components.

Physical-based methods are extensively applied, with the multiconductor transmission lines (MTL) theory being the most prominent one. MTL builds lumped circuits based on individual turns. Currently, there are two main simplification approaches. The first is to create an equivalent circuit using a pure capacitance network, neglecting the influence of inductance by assuming that the inductance value is much larger than the capacitance value [24], [25]. Another is based on energy conservation, where voltage distributes linearly over the inductance, and capacitance is obtained from the total electrical energy [26], [27]. Zhao et al. [28] offered valuable insights into the applicability of these two methods. Although intuitive, these models become challenging to build and solve as the complexity of component structures increases. To address this issue, models based on physical principles have been introduced, considering additional details such as circuit connectivity, fringe fields, and voltage potential [29], [30], [31]. These models offer improved accuracy and practicality by incorporating more physical information and refining equivalent networks. However, the above models are limited to predict the first resonance point and voltage distribution. They cannot handle calculations for the second resonance point, which has been demonstrated to be strongly related to the HFVO within the windings.

Existing models primarily focus on HFVO at the transformer ports, overlooking the potential for more severe voltage oscillations occurring within the transformer. Current research lacks a comprehensive understanding of the underlying mechanisms and the flexible suppression method. Cui et al. [32] investigated voltage oscillation in dual active bridge (DAB) converters based on time-domain analysis. Sekhar et al. [33] proposed connecting a capacitance across the switches to suppress the oscillation. The zero-voltage time is adjusted to eliminate the selected harmonic and the resulted HFVO at the port of transformer, which exhibits effectiveness in modular multiactive bridge converters [34]. However, the ultrahigh switching speed of WBG devices can also result in severe HFVO inside the winding. Cremasco [35] first discovered the more severe voltage spikes within the winding than at the port. However, it lacks a theoretical base for the mechanism of HFVO and a practical oscillation mitigation method. The typical waveform of the oscillation is illustrated in Fig. 1. It can cause a more serious total discharge amplitude, as shown in Fig. 1(c), which has been proven to be inversely proportional to partial discharge lifetime [12]. Moreover, partial discharge caused by HFVO can lead to early breakdown. Therefore, it is imperative to clarify the mechanisms of internal oscillations and propose practical solutions based on these insights.

This article first reveals the mechanism behind the HFVO inside the transformer, the source of the related resonant energy, and how the output voltage affects it. Based on this, some methods to suppress oscillations are proposed. The contributions of this study are outlined as follows.

1) The electrical energy stored in the core is considered, which can improve the accuracy of predicting the oscillation. A simplified circuit is used to obtain the intuitive oscillation mechanism of HFVO.

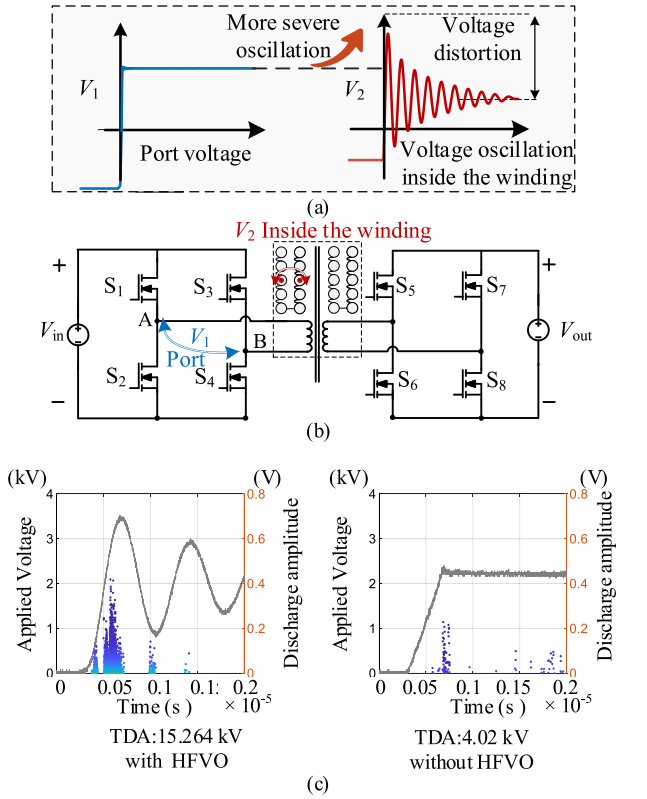

Fig. 1. Schematic of voltage oscillations within the winding. (a) DAB transformer port voltages and oscillation occurring between transformer layers that are more severe than the ports. (b) DAB circuit using a double-winding transformer. (c) Severe partial discharge in the polyimide film occurs under a 1 kHz voltage due to HFVO.

2) An analytical expression for HFVO is proposed, which factors in waveform and physical structure of the transformer, enabling the prediction of winding voltage spikes, ringing frequencies, and amplitudes.
3) The mechanism of HFVO is investigated. For the first time, it is discovered and proved that the resonant magnetic field energy causing HFVO originates from the leakage magnetic energy within one side of the winding rather than the traditionally believed leakage inductance from an imperfect coupling on both sides.
4) Based on the discovered oscillation mechanism, a practical and flexible oscillation suppression process is proposed, including factors related to transformer structure and circuit adjustment methods.

The rest of this article is organized as follows. Section II introduces the modeling and calculating methods of the proposed model. Based on the model, the analytical expression for HFVO is derived in Section III, along with the proposed mechanism and suppression methods. Section IV presents the experimental waveforms of HFVO and verifies the mitigation methods. Finally, Section V concludes this article.

II. Modeling Method and Parameter Calculation

In this section, the issues faced in ordinary MTL models will be addressed. The equivalent circuit will be simplified using

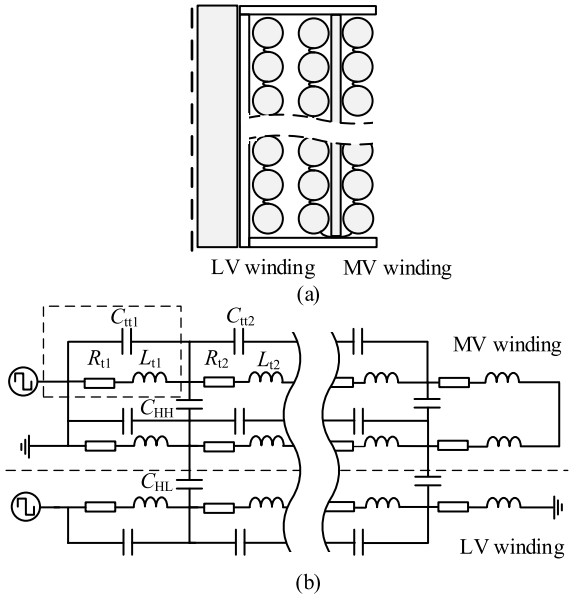

Fig. 2. Basic structure of a high-frequency transformer and the corresponding MTL model. (a) Cross section of the transformer. (b) MTL model, where C_{tt} is interturn capacitance, R_{tk} ($k = 1, 2, \ldots$) is the resistance of each turn, C_{HH} is the interlayer capacitance, and C_{HL} is the interwinding capacitance.

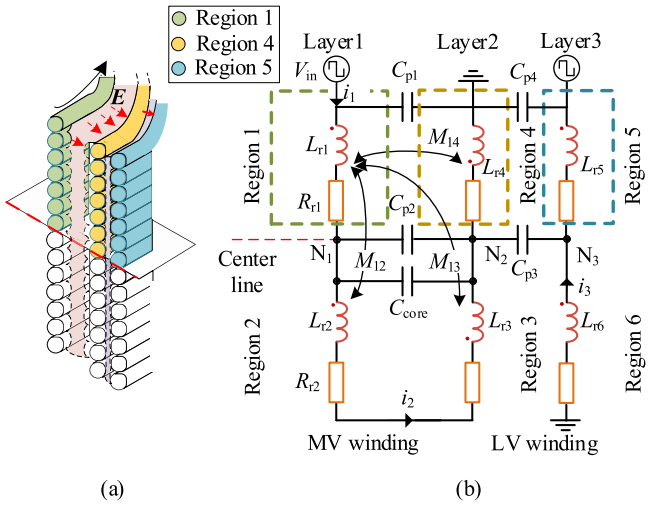

Fig. 3. (a) Dual-winding transformer, with the LV winding consisting of one layer with 14 turns, and the MV winding consisting of two layers with a total of 28 turns. (b) Equivalent circuit model simplified by partitioned energy method. The MV winding is connected in series from region 1–4, while the LV winding is connected in series with region 5 and region 6. As a result, this transformer can be reduced to a simplified configuration with 4 regions in the MV side and 2 regions on the LV side.

the partitioned energy method. Furthermore, the electric field energy within the core will be considered.

A. Ordinary MTL Model

As shown in Fig. 2(a), a transformer is used as a sample with a two-layer primary winding and a single-layer secondary winding. Assuming that the electromagnetic wavelength is much larger than the length of a single turn winding, the ordinary MTL model can be built, as depicted in Fig. 2(b), which includes adjacent interturn capacitance C_{tt}, self-inductance L_t, self-resistance of each turn R_t, and the capacitance between adjacent winding layers C_{HH} or C_{HL}.

Although this model can accurately calculate the first resonance and the corresponding voltage distribution before the frequency [28], it still faces several issues.

1) The equivalent circuit shown in Fig. 2(b) becomes more complex as the number of turns increases.
2) Since the coupling coefficient is ignored, it is unsuitable for calculating frequencies above the first resonance point.
3) The electrical energy of the core is usually neglected, but its influence becomes more significant as the frequency increases.

B. Model Based on the Partitioned Energy Method

The partitioned energy method is used to solve the increasing complicity with the number of turns. The energy of the winding is partitioned into different regions, and each part is represented separately using lumped components, as shown in Fig. 3. This allows the model to be simplified unconstrained by the number of turns.

There are several ways to divide the regions. As the HFVO within the winding is of interest, and as will be shown later, the most severe oscillations occur in the center of the winding. Therefore, each winding layer is divided into upper and lower regions along the center line to capture the severest HFVO within the winding. The detailed modeling method is as follows.

Step 1: Divide the transformer into regions. A transformer with n_l winding layers is divided into n_l parts. Each layer-part is further divided into upper and lower regions along the centerline, resulting in $2n_l$ regions.

For a layer with n_t turns, if $n_t = 2m$, where m is a positive integer, then each of the upper and lower regions contains m turns. If $n_t = 2m$-1, the upper and lower regions contain m and m-1 turns, respectively.

Step 2: The magnetic field coupling between regions is represented as self and mutual inductance (L_r, M). Consider each region as a single winding and calculate the inductance and coupling coefficient of each region using FEM. Then, the resistance R_t of each region is calculated.

Step 3: The interlayer electric field is represented as capacitance C_p. Discretize adjacent windings into infinite tiny capacitors and calculate the equivalent interlayer capacitance C_p based on the assumed linear voltage distribution.

Step 4: The electric field energy generated by the induced electric field inside the magnetic core is equivalent to C_{core} connected between layers.

As an example, the transformer shown in Fig. 3 can be divided into 3×2 regions, with each region containing 7 turns. Then, the calculation methods for each parameter are detailed below.

1) Mutual Inductance: The double two-dimensional (2-D) FEM [32], [36] is used to calculate the mutual inductance between different regions. It decomposes an asymmetric model into two 2-D models. As shown in Fig. 4, sections A and B are formed by cutting through the center of the transformer along the ***zy*** and ***xz*** planes. And the electromagnetic field energy within

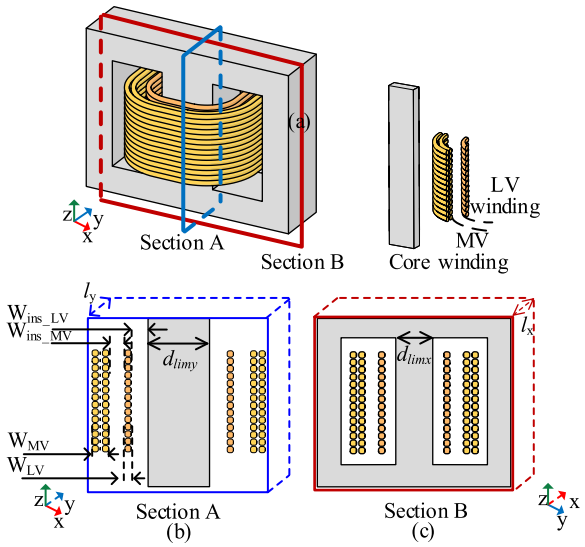

Fig. 4. Concept of double 2-D Model. (a) Three-dimensional model of the high-frequency transformer, (b) and (c) represent the 2-D cross sections of Section A and Section B, respectively.

the 3-D model can be separated and added. The mean turn length MTL is first determined

$$MTL = 2\left(d_{libx} + d_{liby}\right) + \pi\left(w_{\text{ins\_LV}} + w_{\text{ins\_MV}} + w_{\text{MV}} + w_{\text{LV}}\right) \quad (1)$$

where d_{libx} and d_{liby} are the thickness of the core columns in the ***x***- and ***y***-directions, respectively. w_{MV} and w_{LV} are the thicknesses of the MV and LV side windings, $w_{\text{ins\_MV}}$ and $w_{\text{ins\_LV}}$ are the widths of the main insulation and the interlayer insulation, respectively. The thickness l_{x} of Section II-B in the 2-D model is defined as

$$l_x = d_{liby}. \quad (2)$$

The thickness l_{y} of Section II-A is then determined based on MTL and l_{x}

$$l_y = 0.5\left(\text{MTL} - 2l_x\right). \quad (3)$$

The leakage magnetic field energy and the coupled magnetic field energy of the two 2-D models can be calculated separately. The total energy is obtained by combining these energies from the two 2-D models. The self-inductance and mutual inductance for the winding regions within each section can be calculated.

2) Interlayer Capacitance: As shown in Fig. 3, two main capacitances are considered in the proposed model, i.e., the capacitance C_{core} corresponding to the electric field energy within the core, as described in Section II-C, and the interlayer capacitance C_{p}. The interturn capacitance and the winding-to-core capacitance are neglected in this model. This is because, in the samples prepared in Section IV, the interturn capacitance is decreased with increasing turns number, and the distance between core and winding is much larger than the interlayer distance, as shown in Table I.

The interlayer capacitance is calculated in detail in [37]. The electric field energy between the winding layers can be divided

TABLE I
PARAMETERS OF HIGH-FREQUENCY TRANSFORMER S0

Rated Frequency	20 kHz
Core type	U-core/A_e=900 mm^2×4
Window	70 mm × 125 mm
Coil type	28:14turns/Cu litz wire
Wire	1500×0.1 mm
Interlayer insulation	Nomex paper 1 mm
Inter-winding insulation	Air 10 mm
Average distance between LV winding and the core	Resin 20 mm

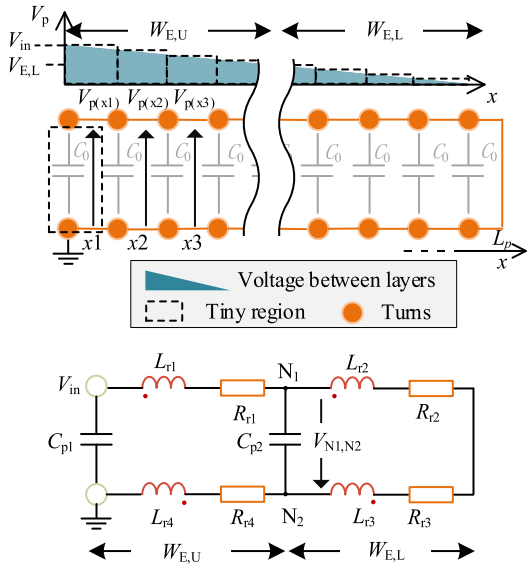

Fig. 5. Variation of interlayer voltage with the position of the winding.

into countless tiny regions, as shown in Fig. 5. Each tiny region can be approximated as a plate. The voltage across each set of plate capacitors is a portion of the interlayer voltage V_{p} (x), which is assumed to distribute linearly along the winding height. Therefore, the electric field energy in each tiny region is

$$W_{\text{tiny}}(j) = \frac{C_0}{2L_p}V_p^2(x_j) \quad j = 1, 2, \ldots m,\ m \to +\infty \quad (4)$$

where x_{j} is the coordinate of the *j*th tiny region along the height of the winding, and V_{p} (x_{j}) is the corresponding interlayer voltage, as shown in Fig. 5 with dashed lines. C_0 is the capacitance value obtained when the winding is considered an equivalent plate capacitor with a height of L_{p}. Furthermore, the electric field energy, $W_{\text{E,U}}$ and $W_{\text{E,L}}$, for the upper and lower regions can be calculated by integrating the electric field energy within these smaller areas. Subsequently, the corresponding capacitances, C_{p1} and C_{p2}, for the two regions are obtained

$$W_{\text{E,U}} = \frac{C_0}{2L_p}\int_0^{L_p/2} V_{\text{p}}^2(x)dx = \frac{7C_0}{48}{V_{\text{in}}}^2 = \frac{C_{\text{p1}}V_{\text{in}}^2}{2} \quad (5)$$

$$W_{\text{E,L}} = \frac{C_0}{2L_p}\int_{L_p/2}^{L_p} V_{\text{p}}^2(x)dx = \frac{C_0}{12}{V_{\text{in}}}^2 = \frac{C_{\text{p2}}V_{\text{N1,N2}}^2}{2} \quad (6)$$

where (5) and (6) represent the electrical energy in the upper and lower layers, respectively, V_{in} is the high-level voltage,

V_{N1N2} is the interlayer voltage in the middle of the winding. The capacitance can then be obtained from these equations.

3) Resistance: The calculating resistance method can be referred to [38], in which a detailed explanation is offered.

C. Electric Energy of Core

The permeability of the core is always considered in the conventional model, which is reflected in the inductance. However, the electric field energy of the core is ignored in the traditional lumped circuit, which can also significantly affect the resonance phenomenon. The widely used MnZn ferrites have a high relative permittivity, reaching 10^4 [39]. In high-frequency converters, complex permeability changes are observed above the resonance point [39]. This is attributed to the relatively small electromagnetic wavelength in MnZn ferrites with high permeability and permittivity, resulting in standing waves on the cross sections [40]. Wunsch et al. [41] used programmable circuit models to calculate the size resonances. The size resonance can also be reflected by electric field energy within the core based on field solutions [42].

Depending on the core parameters, the phenomenon occurs at lower frequencies, such as in the hundreds of kilohertz range. In contrast, HFVO oscillation frequencies are typically higher, reaching into the megahertz range. Therefore, it is necessary to consider the effect of core capacitance.

There is significant flux variation within the core for transformers operating under square waves. Electric energy is generated due to the induced field within the core and the high dielectric constants as

$$W_E = \frac{\varepsilon}{2}\iiint_{V\,\mathrm{core}} |E|^2 dv \tag{7}$$

where W_{E} is electrical energy, ε is the permittivity of the core, and V_{core} is the volume of the core. The induced electric field $\boldsymbol{E}$ can be derived through the magnetic flux within the core. The equivalent magnetic circuit of the EE-type core is shown in Fig. 6. R_0 and R_1 are the magnetic reluctances of the middle and side columns, respectively, while Φ_0 and Φ_1 are the magnetic flux of the middle and side columns, respectively. Typically, the magnetic flux and reluctances of the two side columns are equal. For transformers operating under square wave, the magnetic flux variation ΔB within the core can be given as follows:

$$\Delta B = \frac{V_{\mathrm{in}} T_s/2}{N A_{\mathrm{e}}} \tag{8}$$

where ΔB is the change of magnetic flux density during the high-level voltage, V_{in} is the high-level voltage, T_s is the square wave period, N is the number of turns in one winding, and A_{e} is the cross-sectional area of the middle column. The circumferential electric field induced by the magnetic flux variation

$$\oint Edl = -\frac{\partial}{\partial t}\int_S BdS. \tag{9}$$

A triangular magnetic flux wave is induced by square wave voltage. Combining (8) and (9), the electric field in the core can

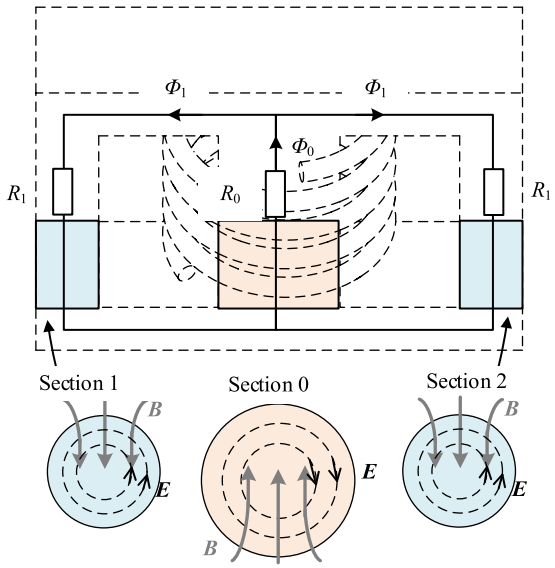

Fig. 6. Schematic diagram of the magnetic circuit of an EE-type core and the induced electric field at different cross sections.

be derived as

$$E(r,t) = -\frac{V_{\mathrm{in}} r}{2A_{\mathrm{e}}N}. \tag{10}$$

Since the magnetic flux is a triangular wave, the induced electric field intensity is a square wave. Then, the electric field energy can be calculated by summing the energy density over the middle and side columns. Generally, for an EE-type magnetic core, the cross-sectional area of the side column and the magnetic flux are half that of the middle column. Therefore, the change in magnetic flux density ΔB can be considered the same. Combining (7) and (10), the electrical field energy of the middle column can be derived as

$$\begin{aligned} W_{E\mathrm{m}} &= \frac{\varepsilon l_{\mathrm{m}}}{2}\iint_{A_{\mathrm{e}}} |E|^2 ds \\ &= \frac{\varepsilon l_{\mathrm{m}} V_{\mathrm{in}}^2 \int_0^{r_{\mathrm{om}}} r^2 \cdot 2\pi r dr}{8A_e^2 N^2} = \frac{\varepsilon l_{\mathrm{m}} {V_{\mathrm{in}}}^2}{16\pi N^2} \end{aligned} \tag{11}$$

where $W_{E\mathrm{m}}$ is the electric field energy of the middle column, l_{m} is the magnetic path length of the middle column, and r_{om} is the radius of the equivalent circle of the middle column section. Similarly, the electric field energy of the side column can be represented as

$$\begin{aligned} W_{Es} &= \frac{\varepsilon l_s}{2}\iint_{A_{\mathrm{s}}} |E|^2 ds = \frac{\varepsilon l_s V_{in}^2 \int_0^{r_{\mathrm{os}}} r^2 \cdot 2\pi r dr}{8A_e^2 N^2} \\ &= \frac{\varepsilon l_s {V_{in}}^2}{16\pi N^2} \cdot \left(\frac{r_{os}}{r_{om}}\right)^4 \end{aligned} \tag{12}$$

where $W_{E\mathrm{s}}$ is the electric field energy of the side column, l_{s} is the magnetic path length of the side column, A_{s} is the cross-sectional area of the side column, and r_{os} is the radius of the equivalent circle of the side column section. This expression can also be extended to parallel cores, where A_{s} represents the cross-sectional area of the single cores. The induced electric field intensity and

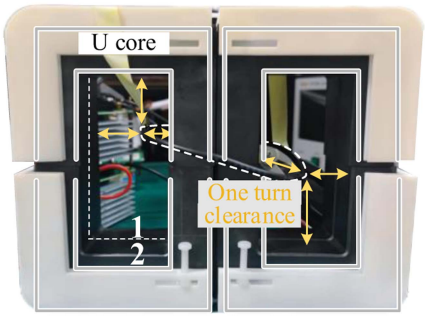

Fig. 7. Core capacitance measurement diagram. To avoid interference from insulation capacitance, a single-turn winding is used, maintaining a specific clearance from the core. The core utilizes a total of 8 U-cores. Four U-cores combine to form one EE-core, with two sets of EE-cores arranged in parallel and labeled on the figure.

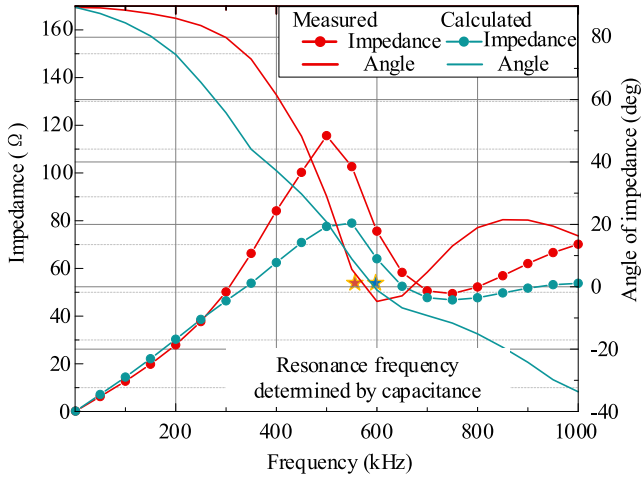

Fig. 8. Impedance characteristics of a single-turn magnetic core considering magnetic core capacitance. In this case, the inductance and capacitance of the computed results are generated through calculations, while the series wire resistance and magnetic core resistance are measured and further taken into account in the computed results.

magnetic field energy are smaller in the side column due to the smaller cross-sectional area and flux, as deduced from (12). This is due to the smaller cross-section limiting the increase in electric field intensity with radius. The induced electric field intensity and magnetic field energy are smaller in the side column due to the smaller cross-sectional area and flux, as deduced from (12). Next, the electric field energy within the core can be obtained, along with the corresponding capacitance C_{core}

$$W_E = W_{Em} + 2W_{Es} = \frac{\varepsilon {V_{\text{in}}}^2}{16\pi N^2}\left[l_{\text{m}} + 2l_{\text{s}}\left(\frac{A_s}{A_e}\right)^2\right] \quad (13)$$

$$C_{\text{core}} = \frac{2W_E}{V_{N1N2}^2} \quad (14)$$

where $V_{N1\,N2}$ is the voltage between N_1 and N_2 in Fig. 3, and for a two-layer winding, $V_{N1\,N2} = 0.5\ V_{\text{in}}$. Furthermore, C_{core} and C_{p2} can be combined into C_{eq}, i.e., $C_{\text{eq}} = C_{\text{p2}} + C_{\text{core}}$. It is noted that the linearity of the core may not be guaranteed in some MV applications, and it can be considered by adjusting the coupling inductance and changing core capacitance.

The experimental setup is shown in Fig. 7, where 8 U-cores are used to form 2 parallel EE-type cores, with the core parameters listed in Table I. A single-turn coil is used, keeping clearance between the coil and the core to avoid the influence of other types of capacitances.

The experimental results are shown in Fig. 8. Theoretically, the impedance of an ideal inductor should increase with frequency. However, an obvious impedance transition is observed. This phenomenon suggests the existence of resonant energy coupling between electric field and magnetic field energies. Due to the distance maintained between the single-turn and the core, the electrical energy should originate from the core. The accuracy of the parasitic capacitance should be verified from the resonance frequency. The amplitude error near the parallel resonance is caused by the error in the impedance angle measured. This is because even minor errors in the impedance angle can result in significant resistance errors under the high impedance induced by parallel resonance, and resistance has a minor effect on the resonance frequency. Furthermore, the calculated and experimental first resonance frequencies are close to each other, which validates the discussion.

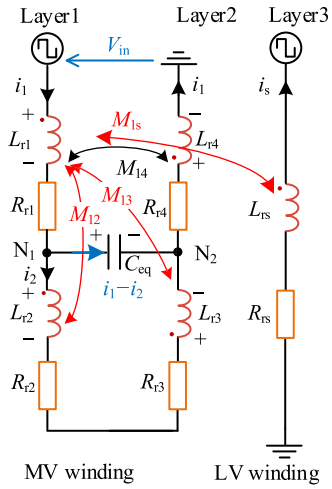

Fig. 9. Simplified circuit model. Compared to Fig. 3, the equivalent capacitance of the core and the interlayer capacitance within the MV side are combined into C_{eq}. The main insulation interlayer capacitance between the MV and LV sides is ignored, as the spacing of the main insulation is usually large. The LV winding is treated as a single winding region. The magnetic coupling represented by red lines is considered nonideal, while the mutual coupling between regions at the same height, represented by black lines, is considered to be ideally coupled in subsequent analyses.

III. Analysis of High-Frequency Oscillation Mechanism and Further Simplified Model

In this section, the analytical expression for HFVO is derived based on the simplified circuit presented in Fig. 9. The HFVO results from series resonance caused by the interaction between the leakage magnetic field energy and the electric field energy within one winding side.

A. Analytical Expression for Voltage Oscillation

The HFVO occurring in the winding can be obtained from the simplified model shown in Fig. 3 using a commercial circuit analyzer. However, it is necessary to derive an analytical expression for the HFVO to find its mechanism and provide methods to reduce it.

The circuit illustrated in Fig. 3 is further simplified, as shown in Fig. 9, to reduce the number of branches. Typically, the midpoint interlayer voltage, V_{N1N2}, experiences the most severe HFVO and is, therefore, calculated to characterize the extent of HFVO within the winding. Due to the larger primary insulation spacing between the MV and LV sides, the interlayer capacitance of the primary insulation is neglected. In Fig. 9, L_{rj} ($j = 1$–4) represents the self-inductance of regions 1–4, and M_{jl} ($j = 1$–4, $l = 1$–4) denotes the mutual inductance between regions. Noted that, in the following derivation, M_{14} and M_{23} are considered to be approximately equal to L_{rj} ($j = 1$–4). This is because M_{23} is the coupling coefficient between two regions at the same height, which is close to 1. Whereas coupling coefficients like M_{13} between regions at different heights are lower, it will be shown later that this type of coupling coefficient determines the leakage magnetic energy of the excitation inductance itself.

The transfer function of the MV side of the transformer can be represented as (see *Appendix A* for a detailed proof)

$$\begin{aligned}\frac{V_{\mathrm{in}}}{i_1} &= sM_{\Sigma 1}(1-\gamma) \\ &\quad + s\left(2M_{\Sigma 4}(1-k)\right)\frac{1/sC_{\mathrm{eq}}}{1/sC_{\mathrm{eq}} + s2M_{\Sigma 4}(1-k)} \qquad (15)\\ M_{\Sigma 1} &= L_{\mathrm{r}1} + M_{12} + M_{13} + M_{14} \\ &\quad + L_{\mathrm{r}4} + M_{14} + M_{24} + M_{34} \\ M_{\Sigma 3} &= M_{12} + M_{24} + M_{13} + M_{34} \\ M_{\Sigma 4} &= L_2 + L_3 + 2M_{23} \approx 4L_{\mathrm{r}1} \\ \gamma &= \frac{M_{\Sigma 3} + \alpha}{M_{\Sigma 4}} \\ \alpha &= \frac{1}{\omega^2 C_{\mathrm{eq}}} \qquad (16)\end{aligned}$$

where k is the coupling coefficient between the MV and LV sides, $M_{\Sigma 1}$ represents half of the magnetizing inductance, $M_{\Sigma 3}$ is the combination of nonideal mutual inductances within the windings, and $M_{\Sigma 4}$ is approximately the sum of self-inductances across four regions. $M_{\Sigma 1}(1\text{-}\gamma)$ signifies the leakage magnetic energy within one side of the winding (the detailed proof is given in *Appendix B*), ω is the electrical angular frequency, and α is small at the resonance frequency, negligible compared to $M_{\Sigma 4}$.

The port's equivalent network can be represented by the series component L_{seq} from the first part of (15), and the parallel component of L_{Meq} and C_{eq} from the second part. In it

$$\begin{aligned}L_{\mathrm{seq}} &= M_{\Sigma 1}(1-\gamma) \\ L_{\mathrm{Meq}} &= 2M_{\Sigma 4}(1-k) \qquad (17)\end{aligned}$$

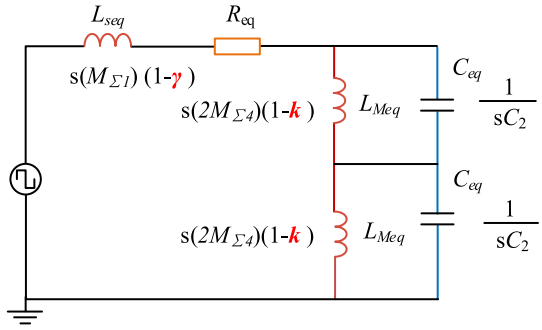

Fig. 10. Proposed decoupling circuit model. L_{seq} is correlated with the leakage magnetic field energy of the MV winding, and L_{Meq} is half of the MV side inductance.

and the circuit shown in Fig. 9 can be equivalently represented as the one in Fig. 10, where the values of the inductances are indicated.

The interlayer voltage at the winding center can be calculated using the voltage drop across C_{eq} in Fig. 9. In the frequency domain, the effect of high-order harmonics of the terminal voltage can be accumulated

$$v_{osc} = \sum_{h}^{N_h}(i_1 - i_2)\frac{1}{\omega_h C_{\mathrm{eq}}} \qquad (18)$$

where N_{h} is the harmonic order, ω_{h} is the harmonic angular frequency, and $i_{1\mathrm{h}}$, and $i_{2\mathrm{h}}$ are the currents in branches 1 and 2, respectively, under the influence of harmonics.

B. Mechanism of Voltage Oscillation

1) Transformer Factor: An equivalent circuit is derived from (15) to investigate the mechanism of HFVO. As shown in Fig. 10, two resonances can be observed in this circuit: parallel resonance occurring between capacitor C_{eq} and the equivalent inductance L_{Meq}

$$L_{\mathrm{Meq}} = 2M_{\Sigma 4}(1-k) \qquad (19)$$

and series resonance occurring between the series inductance L_{seq}

$$L_{\mathrm{seq}} = sM_{\Sigma 1}(1-\gamma) \qquad (20)$$

and capacitor C_{eq}.

HFVO is the overvoltage phenomenon caused by series resonance. As seen in Fig. 10, L_{seq} and C_{eq} form a series resonance, which is the cause of HFVO. The value of L_{seq} is usually smaller than that of L_{Meq} because the insulation spacing between the MV and LV windings is larger, resulting in a smaller coupling coefficient than that between regions within the MV winding. Therefore, parallel resonance occurs before series resonance, and the effect of L_{Meq} can be ignored during series resonance. It can be concluded that HFVO is caused by the series resonance of L_{seq} and C_{eq}.

L_{seq} reflects the leakage magnetic energy within the high-voltage winding (mathematical proof in *Appendix B*). It is worth noting that this energy is independent of the coupling coefficient

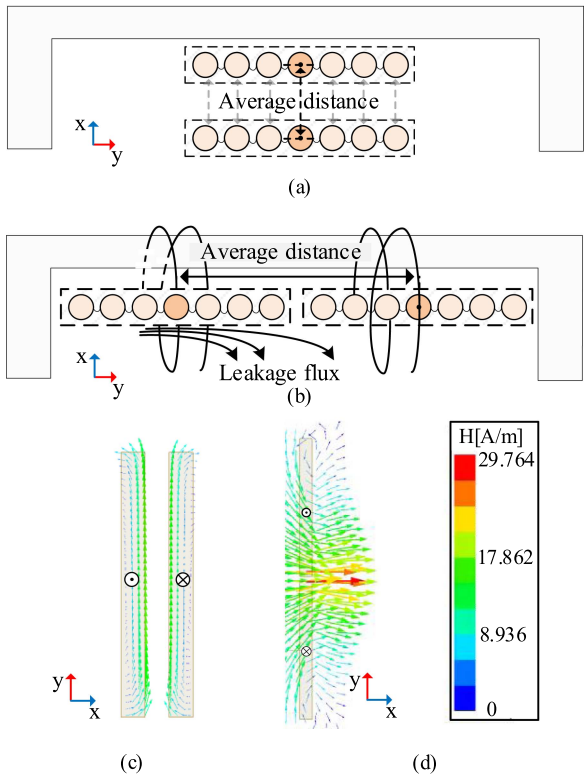

Fig. 11. Impact of winding configuration on leakage magnetic energy. (a) Two winding regions are arranged in the direction of window width ***y***. (b) Two winding regions are arranged in the direction of window height, ***x***. (c) and (d) are the schematic diagrams of magnetic field strength for arrangements (a) and (b), respectively. In (a) and (b), the average distance between turns can be represented by the center distance of both regions, i.e., the distance between the bright circles.

k between the MV and LV windings. Conversely, the traditional leakage inductance, which reflects the coupling extent between the MV and LV windings, is only related to parallel resonance. This is consistent with the experimental results shown in Fig. 18, indicating that when measuring the MV side, the open and short circuits on the LV side only affect the parallel resonance without affecting the series resonance. Therefore, L_{seq} is affected by the winding arrangement on one side.

The winding configuration affects the coupling coefficient between regions, thereby influencing L_{seq}. Considering only the MV side operating as an inductor, its 2-D schematic is shown in Fig. 11. The leakage magnetic energy is distributed in the window and can be represented as

$$W_{\mathrm{leakge}} = \frac{\mu_0}{2} \int_{A_w} H^2 ds \tag{21}$$

where μ_0 is the magnetic permeability of air, A_{w} is the window area, and $\boldsymbol{H}$ is the magnetic field strength of the window. The windings configuration affects the average distance between turns and the leakage magnetic loop, thereby changing the leakage energy reflected by L_{seq}. Smaller numbers of turns are beneficial for reducing leakage energy reducing the average distance between turns. However, the magnetizing inductance has a minimum requirement.

Fig. 11 shows the impact of winding arrangement on leakage energy under the same number of turns and core. As shown, the MV winding has 14 turns. Dividing 14 turns into two regions, when arranged in the window width direction ***x***, as shown in Fig. 11(a), the average distance between turns is 10 mm, and the coupling coefficient is 0.99973 according to *ANSYS*. Conversely, arranging the two regions in the direction of winding height ***y,*** as shown in Fig. 11(b), the average distance is 56 mm, and the coupling coefficient is 0.99817. Calculate the L_{seq} for both arrangements as 65.95 nH and 9.45 nH using (20). Therefore, reducing the average distance between regions in the winding can reduce L_{seq}. The corresponding mechanism is shown in Fig. 11(c) and (d). One ampere of current flows through the two regions in opposite directions. Then, the field within the window can be considered a leakage field contributing to L_{seq}. As can be seen, the field in Fig. 11(c) is much smaller than the other arrangement.

On the other hand, achieving a closer height and width of the winding cross section can result in a lower average distance. However, due to the available core window shape, most reported transformer designs tend to use a configuration where the winding height is much greater than its width, which is not conducive to reducing leakage magnetic energy. Therefore, under the available core window and insulation constraints, making the aspect ratio of the winding closer to the square is beneficial for reducing L_{seq}.

C_{eq} consists of the interlayer capacitance C_{p} and the equivalent core capacitance C_{core}. It contributes to both types of resonance. C_{p} only needs to consider the interlayer capacitance within the MV side without considering the electric field coupling between the MV and LV windings, which will be verified in the subsequent experimental samples S1 and S2. Properly reducing the area of the interlayer plates can suppress voltage oscillations, while the insulation distance between layers needs to be balanced against its impact on L_{seq} and C_{eq}.

2) Circuit Factor: Series resonance is the pathway through which HFVO occurs, and the resonance-related harmonics of the port voltage are the source of HFVO. In conventional bridge converters, the port voltage of the transformer is square-wave and has plentiful harmonic. Under the influence of series resonance, a series of high-frequency harmonics at the port are amplified within the winding, resulting in the HFVO. The transformer S0 shown in Fig. 17 is used to prove this conclusion. Then, the port voltage is decomposed into 70 harmonics using FFT and cumulatively summed from the fundamental frequency. Meanwhile, the variations in the interlayer voltage are shown in Fig. 12. The figure shows the ratio between the midpoint interlayer voltage $V_{7\text{–}22}$ and the port voltage. The ratio starts to increase slowly from 0.5. The rising rate of ratio is maximum at the resonance frequency and becomes rapidly slower towards the two sides. After the resonance point, the rising rate slows and converges to a specific value. This proves that harmonics are amplified inside the transformer by the effect of series resonance, resulting in the HFVO.

The series resonance frequency should be increased through the transformer design to suppress the voltage oscillations, thus reducing the voltage amplification effect. At the same time,

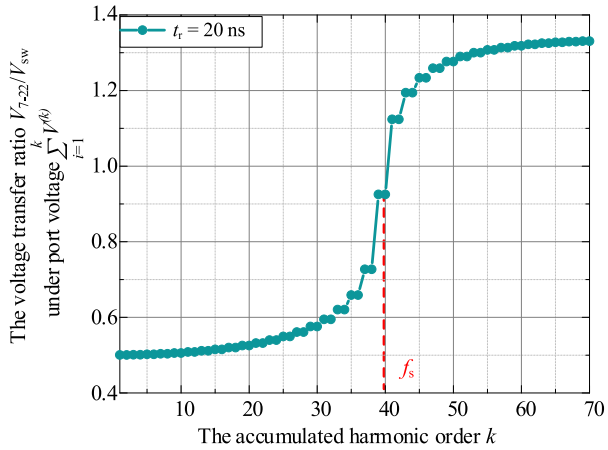

Fig. 12. Midpoint voltage gain after gradual accumulation of higher harmonics V_{7-22}/V_{sw}. The port voltage V_{sw} is at 100 kHz with a t_r of 20 ns. V_{7-22} represents the interlayer voltage between the 7th and 22th turns, as shown in Fig. 14(c), which corresponds to the interlayer voltage at the center of the winding. This voltage can be calculated from the voltage across C_{p1}, as shown in Fig. 9.

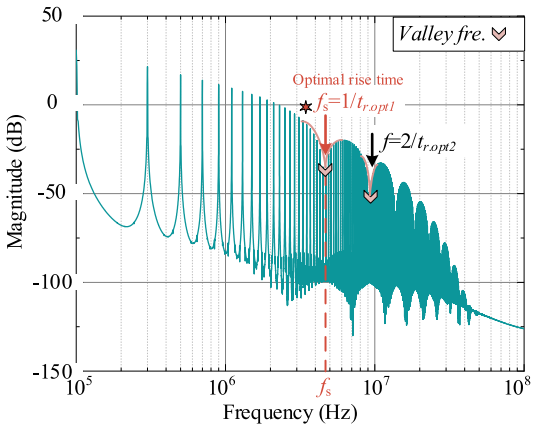

Fig. 13. FFT spectrum of a square wave with $t_r = 20$ ns. Usually, a longer t_r means lower harmonic content, but on the spectrum, there are some harmonic valleys dependent on t_r.

harmonics in the terminal voltage near the series resonance frequency should be suppressed to alleviate voltage oscillations as much as possible.

As discussed previously, the oscillations between the winding layers are caused by the harmonics gained by series resonance. For a two-level square wave with frequency f, voltage-changing time t_r, its FFT decomposition can be expressed as

$$\frac{\hat{v}_h}{\hat{v}} = 2\frac{\sin(h\pi/2)}{h\pi/2}\frac{\sin(h\pi t_r f_1)}{h\pi t_r f_1}, h = 1, 2, 3, \ldots. \quad (22)$$

As shown in Fig. 13, increasing t_r, lowers the envelope of the spectrum. This typically indicates lower levels of higher order harmonics and HFVO. However, it is not feasible to reduce the HFVO by minimizing t_r, as this will reduce the efficiency of the device.

This competition can be alleviated by certain characteristics in the spectrum. Specifically, there are several valleys in the

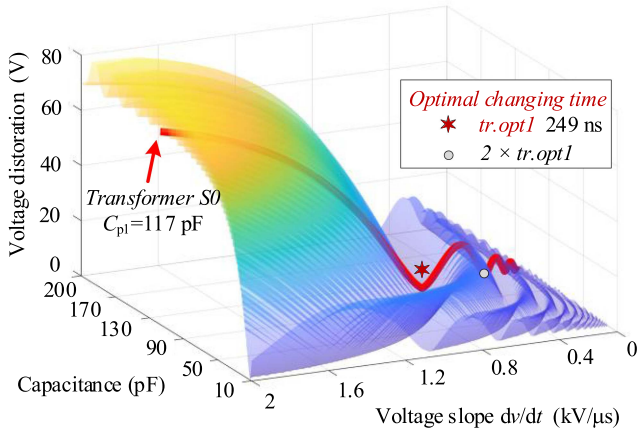

Fig. 14. Voltage distortion versus equivalent capacitance C and voltage slope dv/dt for transformer S0. Voltage distortion is the difference between the peak oscillation value of V_{7-22} and the voltage without oscillation. Valleys appear in the figure and can be used to mitigate oscillations.

spectral characteristics where the harmonic content decreases significantly, as shown in Fig. 13. The first valley frequency is $1/t_r$, and the second valley frequency is $2/t_r$. Since the voltage amplification effect is most significant at harmonics near the series resonance f_s, the HFVO can be mitigated by adjusting the valley frequency to f_s. This characteristic means that faster switching speeds may result in lower harmonic content over a given frequency range.

The HFVO inside the winding under different capacitance and voltage slopes is shown in Fig. 14. The red line represents the voltage distortion of sample S0 for different voltage changing times. The voltage distortion shows a clear nonlinear relationship with the voltage changing time. The tendency is wave-like, caused by the discrete valley frequency. Multiple voltage oscillation minima occur with decreasing voltage changing time. Therefore, HFVO can be reduced by adjusting the voltage changing time to be the reciprocal of valley frequency f_s.

Therefore, if the voltage oscillation after transformer structure optimization proposed in (1) *Transformer factor* does not meet the required, the voltage changing time should be adjusted towards the optimized time in two-level voltage. On the other hand, optimizing the transformer structure can suppress series resonance and increase the resonance frequency f_s. This can reduce the optimized voltage change time ($t_{r.opt} = 1/f_s$), thus mitigating oscillations while minimizing the impact on efficiency.

This method is suitable for half-bridge inverters and hard-switching conditions. However, the switching loss would increase, if the optimal voltage-changing time exceeds the normal value, which degrades the performance of the device. Therefore, a loss-friendly solution is required.

The oscillations can be mitigated by adjusting the switching delay of the three-level voltage. The zero-voltage time induced is adopted to mitigate the port oscillations, which can also be used for the inner HFVOs [35]. As shown in Fig. 15(a), according to the superposition theorem, the three-level output voltage can be considered a superposition of the first switching voltage V_{sw_p1} and the second switching voltage V_{sw_p2}. Each switching action

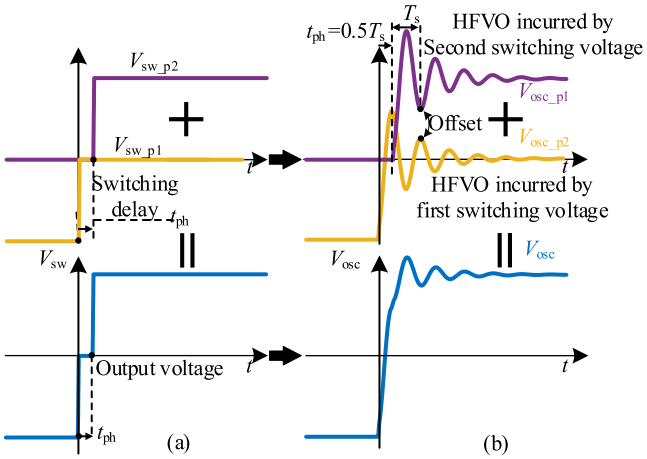

Fig. 15. Schematic of the superposition of the three-level voltage and resulted oscillations. (a) Three-level voltage can be decomposed as a first switching voltage $V_{\mathrm{sw\_p1}}$ and a second switching voltage $V_{\mathrm{sw\_p2}}$. (b) Voltage oscillations induced by $V_{\mathrm{sw\_p1}}$ and $V_{\mathrm{sw\_p2}}$ are $V_{\mathrm{osc\_p1}}$ and $V_{\mathrm{osc\_p2}}$, respectively.

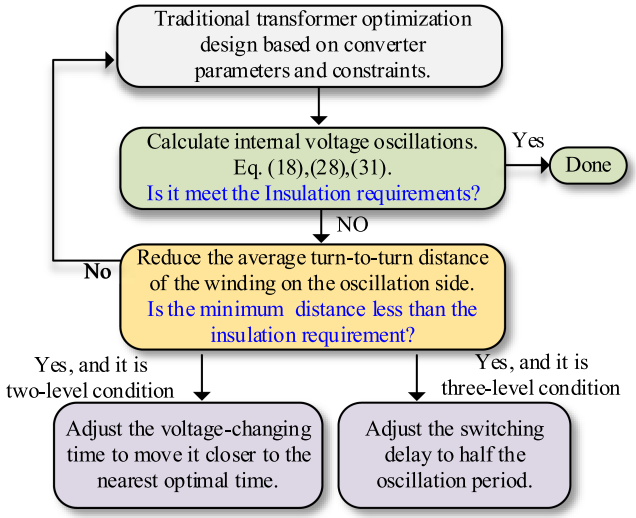

Fig. 16. Flowchart of high-frequency voltage oscillation inside the transformer.

can cause oscillations in the transformer $V_{\mathrm{ocs\_p1}}$ and $V_{\mathrm{ocs\_p2}}$ with the same oscillation period T_s, respectively, as shown in Fig. 15(b). The oscillations caused by the three-level voltage are the superposition of $V_{\mathrm{osc\_p1}}$ and $V_{\mathrm{osc\_p2}}$. Then, the oscillation amplitude of the transformer V_{osc} is determined by the switching delay, t_{ph}. When $t_{\mathrm{ph}} = 0.5T_s$, the high-frequency harmonic of $V_{\mathrm{osc\_p1}}$ and $V_{\mathrm{osc\_p2}}$ has a 180° phase shift and is compensated by each other. Therefore, the oscillation can be mitigated. Compared to the method of adjusting the voltage-changing time, this method does not affect the switching loss due to no additional loss during the zero-voltage time. The limitation is that it is only suitable for three-level conditions. Besides, the control complexity increases since the zero-voltage time is also used to optimize other objectives, such as zero-voltage switch range and current stress [43].

3) HFVO Mitigation Process: To suppress voltage oscillations, one can suppress the internal series resonance of the transformer or adjust the voltage waveform. Suppressing series resonance can increase the resonance frequency and reduce the amount of port harmonics near the resonance frequency. However, transformer structures are often limited by size and core structure and the freedom for optimization is limited. If the voltage oscillation cannot meet the requirements by the transformer design, the HFVO should be suppressed by adjusting the voltage waveform.

For two-level conditions, the internal voltage oscillations can be eliminated by adjusting the voltage changing time to remove specific harmonics. However, this method affects switching losses

In the three-level case, the switching delay can be adjusted according to the oscillation period. The advantage of the above methods is the flexibility in eliminating HFVO without being limited by transformer structure, making the elimination methods complementary for different situations.

The flow of suppressing voltage oscillations is shown in Fig. 16. After traditional transformer design, internal oscillations can be calculated, as described in Section III-A. First, consider reducing the average turn-to-turn distance in the winding on the oscillation side. When constraints like the window fill factor or insulation spacing prevent further changes to the winding structure, try to adjust the voltage changing time for two-level conditions or regulate the zero-voltage time in three-voltage-level conditions. It should be noted that although the requirements may not be met solely by the transformer design, the mitigated series resonance is beneficial for further suppression methods. Since the optimal voltage-changing time or zero-voltage time is the reciprocal of the resonance frequency, increasing the resonance frequency can achieve a faster optimal voltage-changing time or smaller zero-voltage time, thereby reducing the impact on system efficiency.

IV. Measurement Validation

A. Waveforms and Distribution of HFVO

In this section, the experimental waveforms and distribution of HFVO within the transformer shown in Fig. 17 are obtained. The transformer S0 consists of an MV winding with two layers/28 turns and an LV winding with a single layer/7 turns. A 3D-printed bobbin is used to offer insulation and ensure winding dimensions. The specifications are given in Table I. The voltage distortion between winding layers is obtained by measuring the voltage leads, as shown in Fig. 17(b). First, the insulation of the litz wire is melted at the soldered point, and then voltage leads are soldered at the point. The lead is a copper wire with a diameter of approximately 0.5 mm and should be oriented parallel to the direction of the magnetic field to reduce interference.

The impedance-frequency characteristics were measured on the MV side, as shown in Fig. 18. As analyzed in Section III, the frequency and amplitude of the series resonance are independent on the LV side. Normally, the primary insulation spacing on the MV and LV sides is large, resulting in minimal electric field coupling. In sample S0, the primary insulation gap is 10 times larger than that within the MV windings. Therefore, the

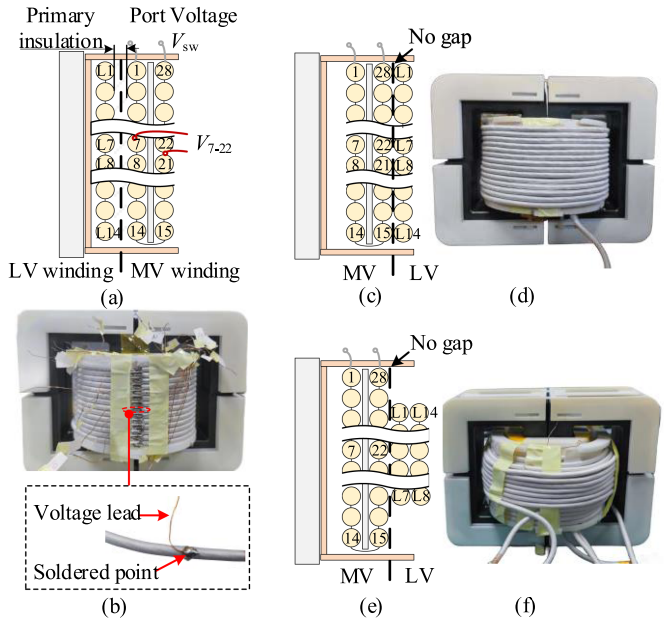

Fig. 17. Schematic and cross-section of the samples (a) the cross section of S0, (b) the photograph of S0 and the measurement method, (c) and (d) are the cross section and photograph of sample S1, (e) and (f) are the cross section and photograph of S2. In S1 and S2, the LV winding is directly wound onto the MV winding with no gap. The voltage between two turns is measured by two voltage leads as shown in (b).

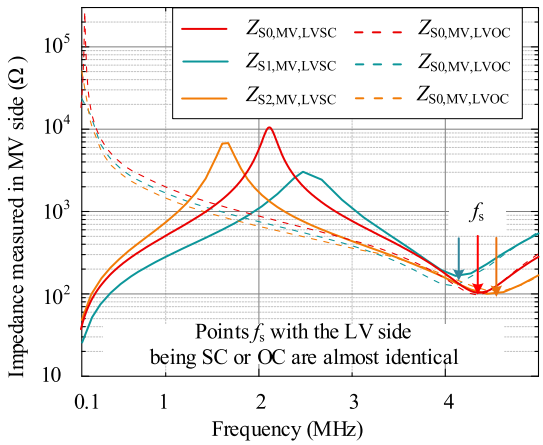

Fig. 18. Impedance-frequency characteristics of the high-frequency transformer sample on the MV side. The series resonance occurs around 4.4 MHz, and it is independent of the state of the low-voltage side. The parameters of sample S0 are presented in Fig. 12 and detailed in Table I. In comparison to S0, samples S1 and S2 differ only in the configuration of LV winding. Specifically, the LV winding of S0 is replaced with a secondary winding directly wound onto the MV winding, without an insulating layer. The secondary winding comprises 14 turns, with S1 having a single-layer secondary winding and S2 having a double-layer secondary winding.

corresponding interwinding capacitance is relatively small and is neglected in the model. To demonstrate that neglecting the electric field coupling between the windings is also reasonable in other structures, samples S1 and S2 are prepared. Compared to S0, the configurations of S1 and S2 differ only in the LV winding configuration. Specifically, in S1 and S2, two windings are placed closely to maximize electric field coupling. The impedance characteristics measured on the MV winding show

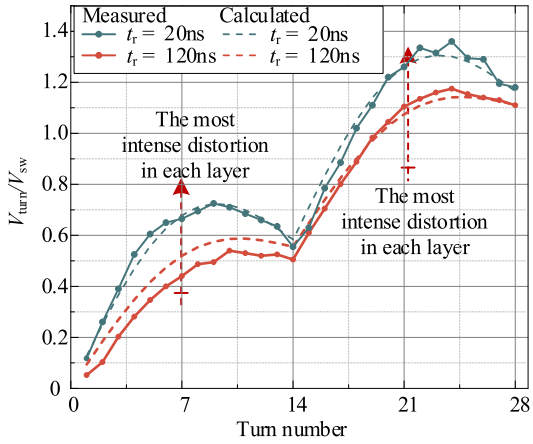

Fig. 19. Voltage distribution along the winding obtained using the circuit shown in Fig. 7 and the experimental results of sample S0. The ground voltage of the 7th and 22th turns is calculated using (15) and (16). Since the oscillating voltage has the highest amplitude at the midpoint and approaches 0 at the ends, a sine fitting is used to fit the ground voltage of other turns as shown by the dashed line.

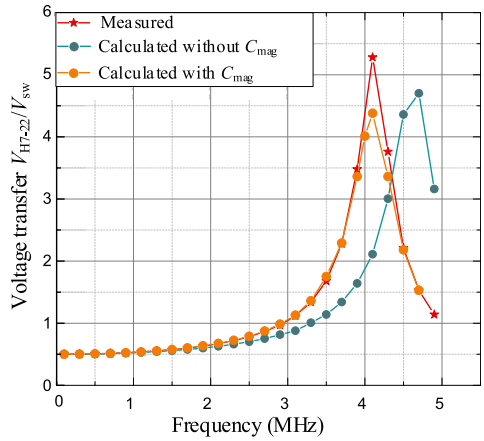

Fig. 20. Frequency response of the voltage gain of the midpoint voltage V_{7-22} in transformer S0. The gain is influenced by the series resonance, reaching its maximum at the series resonance frequency. Compared to the experimental results, the calculations considering the core capacitance provide a more accurate result.

that the electric coupling of both windings slightly affects the series resonance. The state of the LV side of the same sample still does not change the series resonance frequency.

The voltage to ground at each turn of the MV winding for different t_r is shown in Fig. 19. The gray line represents the conventionally assumed linear voltage distribution. When a square wave is applied to the transformer terminal, there is a severe distortion of the voltage inside the winding. The distortion is most significant at the center of each layer, causing the voltage distribution along the winding to deviate from the linear distribution. Additionally, the distortion caused by faster switching times is more severe. Thus, the voltage waveform predicted by the model proposed in this article for the midpoints of the layers accurately reflects the maximum voltage distortion generated within the transformer.

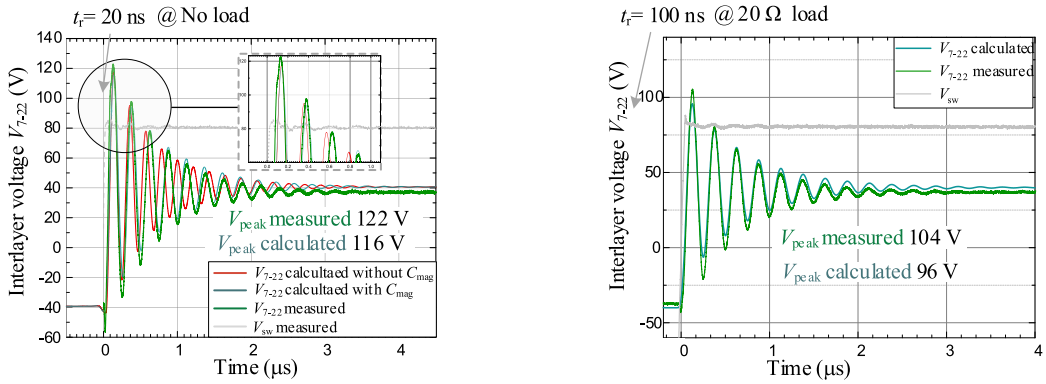

Fig. 21. Voltage oscillations occurring between turns 7 and 22 of the MV side in sample S0 obtained through measurements and calculations. The frequency of these oscillations is 4.1 MHz. The calculated results considering the magnetic core capacitance provide a more accurate oscillation frequency.

The voltage transfer ratio between the midpoint voltage of the layers $V_{7–22}$ and the port voltage in the transformer V_{sw}, denoted as $V_{7–22}/V_{sw}$, is shown in Fig. 20. As the frequency increases from the fundamental frequency to the series resonance frequency, the voltage transfer ratio gradually increases from 0.5. Consequently, the midpoint voltage also rises from half of the port voltage, resulting in the voltage distortion shown in Fig. 19. Thus, the gain of the voltage transfer function around f_s can determine the strength of HFVO. Furthermore, neglecting the magnetic core capacitance leads to overestimating the resonance frequency. This signifies the impact of magnetic core capacitance on HFVO.

The voltage waveform of $V_{7–22}$ and port voltage V_{sw} ($V_{1–28}$, represented by the gray line) were observed using a Tektronix scope, as shown in Fig. 21. This shows a significant oscillation occurred inside the transformer. The peak voltage at the midpoint between layers reaches approximately 1.5 times the peak voltage of V_{sw}, which is around three times the midpoint voltage of a normal linear voltage distribution. Furthermore, the resonance frequency is the same for load and no-load conditions, since the operating conditions on the LV side do not affect the series resonance. However, the load current induces a longer t_r, resulting in different oscillation amplitudes.

The above phenomenon confirms the conclusion made in Section III, that HFVO is caused by the amplification of harmonics near the resonance frequency in the output voltage due to series resonance.

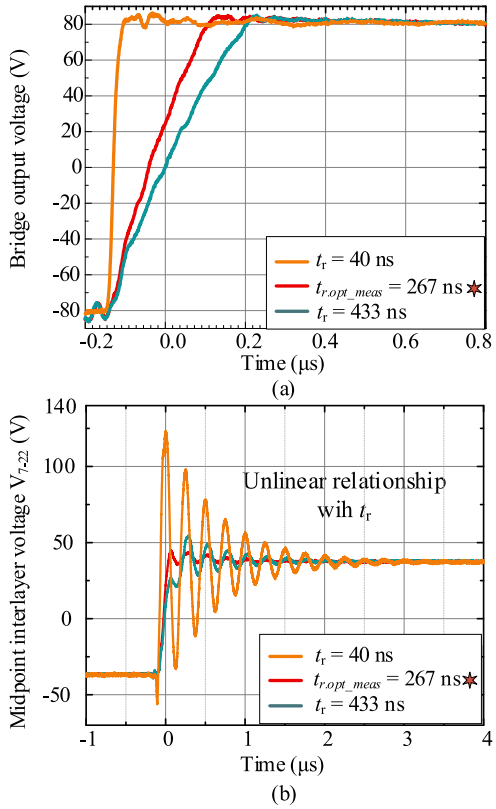

Fig. 22. Waveform of HFVO with adjusting the square voltage t_r. (a) V_{sw} waveforms with three different t_r. (b) Corresponding waveform of interlayer voltage $V_{7–22}$.

B. Mitigation Methods for Adjusting the Voltage Waveform

The HFVO can be mitigated by adjusting the voltage changing time of the two-level voltage or regulating the switching delay of the three-level voltage. First, the former method is validated at a half-bridge inverter, with S0 as an example. The voltage changing time is adjusted by the gate resistance for hard-switching condition. The optimum switching time, $t_{r.opt1}$, is obtained as 249 ns from Fig. 14. Different voltage changing times are shown in Fig. 22(a). The corresponding voltage waveforms $V_{7–22}$ are shown in Fig. 22(b). Therefore, the oscillations can be mitigated by selecting the optimal switching time, rather than selecting a longer switching time.

Afterward, the mitigated HFVO is achieved by regulating the switching delay time of three-level voltage. It is validated at a full-bridge inverter, with a 10 Ω resistance load at the LV side of the transformer. Due to the 70 μH leakage inductance of Sample S0, the voltage leads to current, and the converter is under soft-switching conditions. The optimal switching delay is half of the oscillation period, 121 ns, as shown in Fig. 23(a). Compared to the two-level voltage, the oscillations of interlayer voltage $V_{7–22}$ are significantly reduced, and switching loss is unaffected by this method due to no additional loss caused in the zero-voltage time.

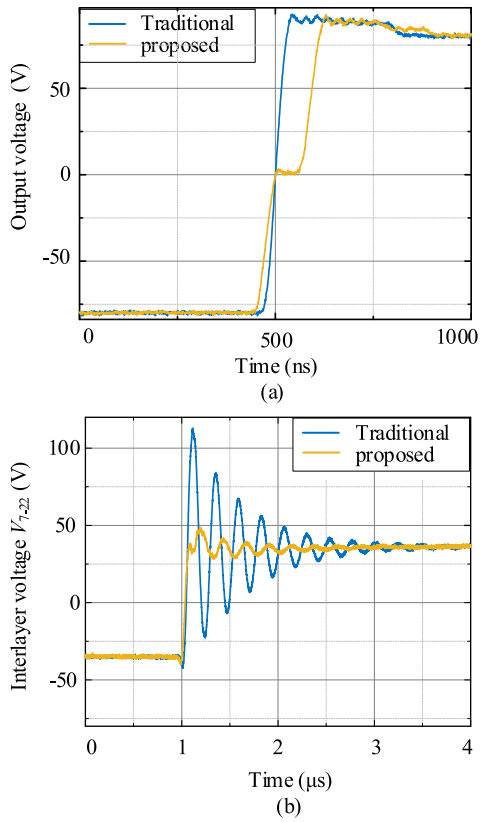

Fig. 23. Waveform of output voltage (a) and the interlayer voltage V_{7-22} (b) for the mitigation method by adjusting the switching-delay time.

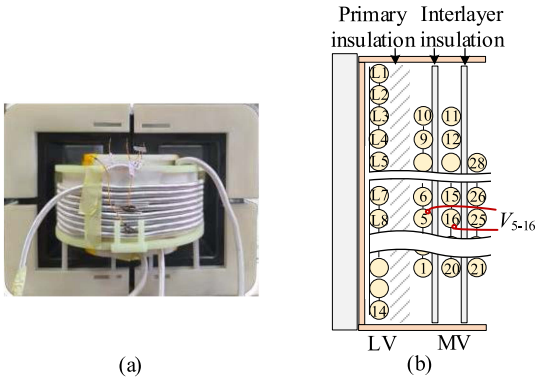

Fig. 24. (a) Photograph of sample S3 and (b) cross section of the transformer. The MV winding of S3 consists of 3 layers with 28 turns. The interwinding distance, interlayer distance, and the core are the same as S0. V_{5-16} indicates the voltage between the midpoints of the first and second layers of the MV winding of S3.

C. Mitigation Method for Decreasing Turn-to-Turn Distance

As discussed in Section III-B, a lower leakage magnetic energy can be obtained by a smaller turn-to-turn distance on one side. A sample S3 is prepared to validate the method, and sample S0 is used to compare, as shown in Fig. 24. The sample S3 and S0 differ in the number of layers on the MV side. The number of layers in S0 is 2, and that of S3 is 3, and the average turn-to-turn distance of S3 is 19 mm, and that of S0 is 29 mm. The voltage

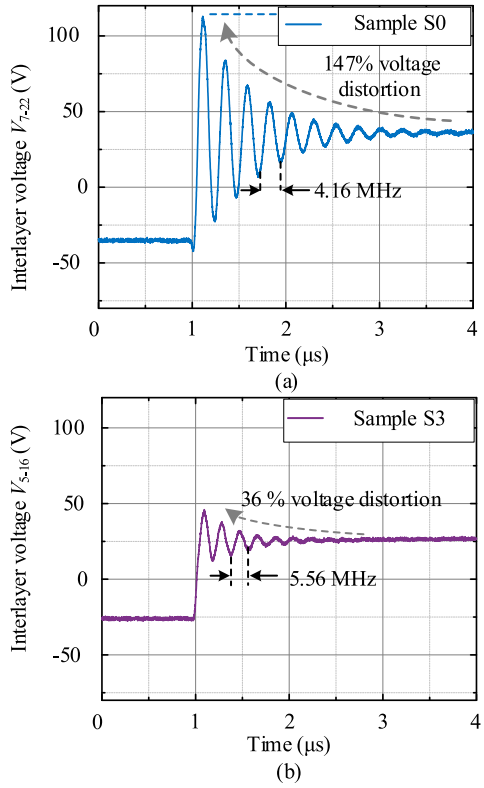

Fig. 25. Voltage suppression effect of decreasing turn-to-turn distance, with mid interlayer voltage waveform of the sample (a) S0 and (b) S3.

waveforms of the mid interlayer are shown in Fig. 25. The oscillation frequency is increased by 33%, and the oscillation is significantly decreased.

The increasing layer number can also reduce the equivalent capacitance. In order to determine the impact of the capacitance and the leakage magnetic energy. The port equivalent capacitance of S0 and S3 are measured at MV port with LV port kept open circuit. The equivalent port capacitance of S3 is 85% of that in S0. As proved in Section III, the HFVOs are caused by the series resonance, which is contributed by the inner leakage inductance and the equivalent capacitance. Then, the leakage magnetic energy of S3 is nearly 65% of that in S0 according to the resonance formula by assuming that the electric energy of S3 is approximately 85% of that in S0. Therefore, oscillation can be mitigated by the reduced leakage magnetic energy in the winding.

V. Conclusion

A comprehensive analysis of the phenomenon, mechanism, and influencing factors of HFVO occurring inside the winding is provided in this article. Based on the partitioned field energy, the internal network of the transformer is simplified into a decoupled circuit, and the analytical expressions for HFVO are derived. The model considers the internal electric field energy of the transformer core for the first time and is experimentally verified to be accurate.

Based on the proposed model, a comprehensive analysis of HFVO is presented. It is pointed out that the cause of HFVO inside the winding is not attributed to imperfect transformer primary-secondary coupling as traditionally thought. Instead, the HFVO inside the winding is due to series resonance caused by the leakage magnetic field energy and electrical energy of one winding, independent of the state of the other winding.

The HFVO suppression methods are proposed based on the discovered mechanism. In terms of transformer design, series resonance can be suppressed by reducing the average turn-to-turn distance of the winding on the oscillation side. Circuitwise, for hard-switching and low-frequency conditions, the voltage changing time in two-level conditions should be adjusted to be inversely proportional to the serial resonance frequency, which can eliminate high-order harmonics associated with series resonance, thereby eliminating oscillations. For three-level conditions, the switching delay time is set to half of the oscillation period to mitigate HFVO. The above suppression methods complement each other, enhancing the flexibility in suppressing voltage oscillations. The experiments validate the effectiveness of the proposed methods.

APPENDIX

A. Port Transfer Function

Noted that, in the following derivation, M_{14} and M_{23} are considered to be approximately equal to L_{rk} ($k=1$–4). This is because M_{23} is the coupling coefficient between two regions at the same height, which is close to 1. Whereas coupling coefficients like M_{13} between regions at different heights are lower, it will be shown later that this type of coupling coefficient determines the leakage magnetic energy of the excitation inductance itself.

Branch currents i_1 and i_2 are then obtained to determine the voltages. The relationship between port voltage and branch current can be expressed as

$$\begin{aligned} V_{\mathrm{in}} &= V_{\mathrm{lr1}} + V_{\mathrm{lr2}} + V_{\mathrm{lr3}} + V_{\mathrm{lr4}} \\ &= \begin{bmatrix} L_{\mathrm{r1}} & M_{12} & M_{13} & M_{14} & M_{1\mathrm{s}} \\ M_{12} & L_{\mathrm{r2}} & M_{23} & M_{24} & M_{2\mathrm{s}} \\ M_{13} & M_{23} & L_{\mathrm{r3}} & M_{34} & M_{3\mathrm{s}} \\ M_{14} & M_{24} & M_{34} & L_{\mathrm{r4}} & M_{4\mathrm{s}} \end{bmatrix} \begin{bmatrix} si_1 \\ si_2 \\ si_2 \\ si_1 \\ -si_{\mathrm{s}} \end{bmatrix} \end{aligned} \tag{23}$$

where the reference directions for voltage and current are shown in Fig. 9. The relationship between i_1 and i_2 can be obtained from the KVL

$$\begin{aligned} U_{Ceq} &= U_{lr2} + U_{lr3} \\ &= \frac{1}{sC_{\mathrm{eq}}}(i_1 - i_2) \\ &= s\left(M_{\Sigma 3} i_1 + M_{\Sigma 4} i_2 - M_{2s} i_s - M_{3s} i_s\right) \end{aligned} \tag{24}$$

$$M_{\Sigma 3} = M_{12} + M_{24} + M_{13} + M_{34} \tag{25}$$

$$M_{\Sigma 4} = L_{r2} + 2M_{23} + L_{r3}. \tag{26}$$

For a transformer with a turns ratio of N, assuming the coupling coefficient between the primary and secondary sides is k, then the nonideal voltage ratio is $N' = kN$, and the relationship between currents in both sides is

$$i_s = 0.5N'(i_1 + i_2). \tag{27}$$

Substituting (27) into (24) results in

$$\begin{aligned} i_2 &= \frac{1/sC_{\mathrm{eq}} - s\left[M_{\Sigma 3} - 0.5N'(M_{2\mathrm{s}} + M_{3\mathrm{s}})\right]}{1/sC_{\mathrm{eq}} + s\left[M_{\Sigma 4} - 0.5N'(M_{2\mathrm{s}} + M_{3\mathrm{s}})\right]} i_1 \\ &= \frac{1/sC_{\mathrm{eq}} - s\left[M_{\Sigma 3} - k^2 M_{\Sigma 4}\right]}{1/sC_{\mathrm{eq}} + sM_{\Sigma 4}(1-k^2)} i_1. \end{aligned} \tag{28}$$

Combining (23), (27), and (28), the transfer function of the transformer port is derived as

$$\begin{aligned} \frac{V_{\mathrm{in}}}{i_1} &= s\left(M_{\Sigma 1} - 0.5N' \cdot M_{\Sigma s}\right) \\ &\quad + s\left(M_{\Sigma 2} - 0.5N' \cdot M_{\Sigma s}\right) \\ &\quad \times \left(\frac{1/sC_{\mathrm{eq}} - s\left[M_{\Sigma 3} - 0.5N'(M_{\Sigma 2s} + M_{\Sigma 3s})\right]}{1/sC_{\mathrm{eq}} + sM_{\Sigma 4} - 0.5N'(M_{\Sigma 2s} + M_{\Sigma 3s})}\right) \end{aligned} \tag{29}$$

where M_{js} ($j = 1$–4) represents the mutual inductance between each region on the MV and LV sides. The mutual inductances are then expressed by self-inductance and coupling coefficient as

$$Mjs = k\sqrt{L_{rj}L_{rs}} = k\sqrt{L_{rj}\left(4/N\right)^2 L_{rj}} = k\frac{4}{N}L_{rj}. \tag{30}$$

Substituting (30) into (29), the transfer function for port voltage and current is represented as

$$\begin{aligned} \frac{V_{\mathrm{in}}}{i_1} = & \overbrace{\begin{aligned} & s\left(M_{\Sigma 4}\left(1-2k^2\right) + M_{\Sigma 3}\right)\left(1 - \frac{s\left[M_{\Sigma 3} - k^2 M_{\Sigma 4}\right]}{1/sC_{\mathrm{eq}} + sM_{\Sigma 4}(1-k^2)}\right) \\ & + s\left(M_{\Sigma 4}\left(1-2k^2\right) + M_{\Sigma 3}\right)\left(\frac{1/sC_{\mathrm{eq}}}{1/sC_{\mathrm{eq}} + sM_{\Sigma 4}(1-k^2)}\right). \end{aligned}}^{\text{Former part}} \end{aligned} \tag{31}$$

Thus, (31) can be divided into two parts, and the former part is further simplified as

$$\begin{aligned} & s\left(M_{\Sigma 4}\left(1-2k^2\right) + M_{\Sigma 3}\right)\left(1 - \frac{\left[M_{\Sigma 3} - k^2 M_{\Sigma 4}\right]}{-\alpha + M_{\Sigma 4}(1-k^2)}\right) \\ & = \frac{-M_{\Sigma 3}^2 + M_{\Sigma 4}^2\left(1-2k^2\right) + 2M_{\Sigma 3}M_{\Sigma 4}k^2}{-\alpha M_{\Sigma 3} + \alpha M_{\Sigma 4}\left(2k^2-1\right)} \\ & \quad \frac{}{-\alpha + M_{\Sigma 4}(1-k^2)} \end{aligned} \tag{32}$$

$$\alpha = \frac{1}{\omega^2 C_{\mathrm{eq}}}. \tag{33}$$

The α in the denominator of (32) can be ignored because it is relatively small compared to the other term. Setting $M_{\Sigma 3} =$

$k_1 \times M_{\Sigma 4}$, (32) can be simplified to

$$\frac{M_{\Sigma 4}^2\left[1-{k_1}^2+k^2\left(2k_1-2\right)\right]+\alpha M_{\Sigma 4}\left[2k^2-\left(1+k_1\right)\right]}{M_{\Sigma 4}\left(1-k^2\right)} \tag{34}$$

where k_1 represents the nonideal coupling coefficient within the windings, usually larger than the coupling coefficient k between the MV and LV sides. Compared to k^2, k_1 is approximately equal to 1, thus (34) can be further simplified to

$$\begin{aligned}
&\frac{M_{\Sigma 4}^2\left(1+k_1\right)\left(1-k_1\right)\left(1-k^2\right)+\alpha M_{\Sigma 4}\left(1+k_1\right)\left(1-k^2\right)}{M_{\Sigma 4}\left(1-k^2\right)} \\
&=M_{\Sigma 4}\left(1+k_1\right) \\
&+\frac{\left(1-k^2\right) M_{\Sigma 4}^2\left(1+k_1\right)\left(-k_1\right)+\alpha M_{\Sigma 4}\left(1+k_1\right)\left(1-k^2\right)}{M_{\Sigma 4}\left(1-k^2\right)} \\
&=M_{\Sigma 4}\left(1+k_1\right)+M_{\Sigma 4}\left(1+k_1\right)\left(-k_1-\frac{\alpha}{M_{\Sigma 4}}\right) \\
&=M_{\Sigma 4}\left(1+k_1\right)\left(1-\frac{M_{\Sigma 3}+\alpha}{M_{\Sigma 4}}\right) \\
&=M_{\Sigma 1}\left(1-\gamma\right)
\end{aligned} \tag{35}$$

where parameter $\gamma = (M_{\Sigma 3}+\alpha)/M_{\Sigma 4}$ represents the leakage magnetic energy of the excitation inductance itself (proof in Appendix II). The latter part of (31) can be simplified to

$$\begin{aligned}
&s\left(M_{\Sigma 4}\left(1+k_1-2k^2\right)\right)\left(\frac{{}^1\!/_{sC_{\mathrm{eq}}}}{{}^1\!/_{sC_{\mathrm{eq}}}+sM_{\Sigma 4}\left(1-k^2\right)}\right) \\
&\approx 2sM_{\Sigma 4}\left(1-k^2\right)\left(\frac{{}^1\!/_{sC_{\mathrm{eq}}}}{{}^1\!/_{sC_{\mathrm{eq}}}+sM_{\Sigma 4}\left(1-k^2\right)}\right) \\
&\approx 2s\left[2M_{\Sigma 4}\left(1-k\right)\right]\left(\frac{{}^1\!/_{sC_{\mathrm{eq}}}}{{}^1\!/_{sC_{\mathrm{eq}}}+s2M_{\Sigma 4}\left(1-k\right)}\right).
\end{aligned} \tag{36}$$

In circuit terms, (36) can be considered as the inductance $2M_{\Sigma 4}(1\text{-}k)$ in parallel with the capacitance C_{eq}.

B. Meaning of L_{seq}

For an ideal inductor, all magnetic flux is contained within the core, and the inductance value is directly proportional to the square of the number of turns. Since the number of turns in the four regions on the high-voltage side is the same, the ideal inductance is given by

$$L_{\mathrm{ideal}} = 4\left(L_{\mathrm{r1}}+L_{\mathrm{r2}}+L_{\mathrm{r3}}+L_{\mathrm{r4}}\right). \tag{37}$$

However, leakage flux exists within the window, and the coupling coefficient between regions is less than 1. Therefore, the effective excitation inductance is smaller and is given by

$$\begin{aligned}
L_{\mathrm{act}} =& \left(L_{\mathrm{r1}}+L_{\mathrm{r2}}+L_{\mathrm{r3}}+L_{\mathrm{r4}}\right) \\
&+2\left(M_{12}+M_{13}+M_{14}+M_{23}+M_{24}+M_{34}\right) \\
\approx& 2\left(L_{\mathrm{r1}}+L_{\mathrm{r2}}+L_{\mathrm{r3}}+L_{\mathrm{r4}}\right) \\
&+2\left(M_{12}+M_{13}+M_{24}+M_{34}\right).
\end{aligned} \tag{38}$$

The difference between (37) and (38) can be regarded as the leakage inductance referred to the high-voltage side

$$\begin{aligned}
L_{\mathrm{lk}} &= L_{\mathrm{ideal}}-L_{\mathrm{act}} \\
&= 2\left[\left(L_{\mathrm{r1}}-M_{12}\right)+\left(L_{\mathrm{r2}}-M_{13}\right)\right. \\
&\quad \left.+\left(L_{\mathrm{r3}}-M_{24}\right)+\left(L_{\mathrm{r4}}-M_{34}\right)\right] \\
&\approx L_{\Sigma 1}\frac{\left[\left(L_{\mathrm{r1}}-M_{12}\right)+\left(L_{\mathrm{r2}}-M_{13}\right)\right.}{\left.+\left(L_{\mathrm{r3}}-M_{24}\right)+\left(L_{\mathrm{r4}}-M_{34}\right)\right]} \\
&= L_{\Sigma 1}\frac{\left(L_{\mathrm{r2}}+L_{\mathrm{r2}}+L_{\mathrm{r3}}+L_{\mathrm{r4}}\right)-M_{\Sigma 3}}{L_{\Sigma 4}} \\
&\approx L_{\Sigma 1}\left(1-\gamma\right)=L_{\mathrm{seq}}.
\end{aligned} \tag{39}$$

REFERENCES

[1] B. Whitaker et al., "A high-density, high-efficiency, isolated on-board vehicle battery charger utilizing silicon carbide power devices," *IEEE Trans. Power Electron.*, vol. 29, no. 5, pp. 2606–2617, May 2014.

[2] J. Ebersberger, M. Hagedorn, M. Lorenz, and A. Mertens, "Potentials and comparison of inverter topologies for future all-electric aircraft propulsion," *IEEE J. Emerg. Sel. Topics Power Electron.*, vol. 10, no. 5, pp. 5264–5279, Oct. 2022.

[3] S. Wang et al., "Multifunction capability of SiC bidirectional portable chargers for electric vehicles," *IEEE J. Emerg. Sel. Topics Power Electron.*, vol. 9, no. 5, pp. 6184–6195, Oct. 2021.

[4] T. Guillod, J. E. Huber, G. Ortiz, A. De, C. M. Franck, and J. W. Kolar, "Characterization of the voltage and electric field stresses in multi-cell solid-state transformers," in *Proc. IEEE Energy Convers. Congr. Expo.*, 2014, pp. 4726–4734.

[5] T. Liu, Q. Li, G. Dong, M. Asif, X. Huang, and Z. Wang, "Multi-factor model for lifetime prediction of polymers used as insulation material in high frequency electrical equipment," *Polym. Testing*, vol. 73, pp. 193–199, Feb. 2019.

[6] M. S. Moonesan, S. H. Jayaram, and E. A. Cherney, "Study on form-wound machine turn insulation subjected to unipolar and bipolar square waves," *IEEE Trans. Dielectrics Elect. Insul.*, vol. 23, no. 6, pp. 3242–3248, Dec. 2016.

[7] R. Agarwal, H. Li, Z. Guo, and P. Cheetham, "The effects of PWM With high dv/dt on partial discharge and lifetime of medium-frequency transformer for medium-voltage (MV) solid state transformer applications," *IEEE Trans. Ind. Electron.*, vol. 70, no. 4, pp. 3857–3866, Apr. 2023.

[8] Y. Zhao, G. Zhang, D. Han, K. Li, Z. Qiu, and F. Yang, "Experimental study on insulation properties of epoxy casting resins using high-frequency square waveforms," *CSEE J. Power Energy Syst.*, vol. 7, no. 6, pp. 1227–1237, Nov. 2021.

[9] L. P. Shang, Q. Bu, H. Xu, and Q. Zhang, "Influence of voltage waveform and duty cycle on solid insulation strength in high frequency transformer," in *Proc. IEEE 6th Int. Elect. Energy Conf.*, 2023, pp. 3323–3327.

[10] T. Guillod, R. Faerber, D. Rothmund, F. Krismer, C. M. Franck, and J. W. Kolar, "Dielectric losses in dry-type insulation of medium-voltage power electronic converters," *IEEE J. Emerg. Sel. Topics Power Electron.*, vol. 8, no. 3, pp. 2716–2732, Sep. 2020.

[11] W. Wang, X. Wang, J. He, Y. Liu, and S. Li, "Dielectric breakdown characteristics of epoxy resin induced by high frequency electric stress used in solid state transformer," in *Proc. IEEE 3rd Int. Conf. Dielectrics*, 2020, pp. 162–165.

[12] Z. Li et al., "Experimental study on the damage mechanism of high-frequency partial discharge of multilayer PI films under repetitive electrical stress," in *Proc. IEEE/IAS Ind. Commercial Power Syst. Asia*, 2023, pp. 1648–1653.

[13] F. Guastavino and A. Dardano, "Life tests on twisted pairs in presence of partial discharges: Influence of the voltage waveform," *IEEE Trans. Dielectrics Elect. Insul.*, vol. 19, no. 1, pp. 45–52, Feb. 2012.

[14] T. Liu, Y. Xiao, Y. Lu, X. Huang, Q. Li, and Z. Wang, "Effect of voltage frequency on surface discharge characteristics and aging process," in *Proc. IEEE Elect. Insul. Conf.*, 2017, pp. 463–466.

[15] M. Khanali, S. Jayaram, and J. Cheng, "Effects of voltages with high-frequency contents on the transformer insulation properties," in *Proc. IEEE Elect. Insul. Conf.*, 2013, pp. 235–238.
[16] X. Zhang, Y. Zhao, S. L. Ho, and W. N. Fu, "Analysis of wireless power transfer system based on 3-D finite-element method including displacement current," *IEEE Trans. Magn.*, vol. 48, no. 11, pp. 3692–3695, Nov. 2012.
[17] P. S. R. Nayak and D. Kishan, "Design and analysis of SS resonant IPT system with computed mutual inductance through FEM model," in *Proc. Int. Conf. Power, Instrum., Control Comput.*, 2018, pp. 1–5.
[18] S. Allirani, H. Vidhya, T. Aishwarya, T. Kiruthika, and V. Kowsalya, "Design and performance analysis of switched reluctance motor using ANSYS maxwell," in *Proc. 2nd Int. Conf. Trends Electron. Inform.*, 2018, pp. 1427–1432.
[19] O. V. Tikhonova and A. T. Plastun, "Electromagnetic calculation of induction motor by 'ANSYS Maxwell'," in *Proc. IEEE Conf. Russian Young Researchers Elect. Electron. Eng.*, 2018, pp. 822–826.
[20] B. Cogitore, J. P. Keradec, and J. Barbaroux, "The two-winding transformer: An experimental method to obtain a wide frequency range equivalent circuit," *IEEE Trans. Instrum. Meas.*, vol. 43, no. 2, pp. 364–371, Apr. 1994, doi: 10.1109/19.293449.
[21] C. Liu, L. Qi, X. Cui, Z. Shen, and X. Wei, "Wideband mechanism model and parameter extracting for high-power high-voltage high-frequency transformers," *IEEE Trans. Power Electron.*, vol. 31, no. 5, pp. 3444–3455, May 2016.
[22] R. Pintelon, P. Guillaume, Y. Rolain, J. Schoukens, and H. Van Hamme, "Parametric identification of transfer functions in the frequency domain-a survey," *IEEE Trans. Autom. Control*, vol. 39, no. 11, pp. 2245–2260, Nov. 1994.
[23] C. Sanathanan and J. Koerner, "Transfer function synthesis as a ratio of two complex polynomials," *IEEE Trans. Autom. Control*, vol. 8, no. 1, pp. 56–58, Jan. 1963.
[24] A. Massarini and M. K. Kazimierczuk, "Self-capacitance of inductors," *IEEE Trans. Power Electron.*, vol. 12, no. 4, pp. 671–676, Jul. 1997.
[25] G. Dong, F. Zhang, Y. Liu, W. Meng, and C. Xu, "Analytical method for extraction of stray capacitance in single-layer CM chokes," in *Proc. IEEE Energy Convers. Congr. Expo.*, 2019, pp. 3185–3191.
[26] H. Zhao et al., "Parasitic capacitance modeling of inductors without using the floating voltage potential of core," *IEEE Trans. Ind. Electron.*, vol. 69, no. 3, pp. 3214–3222, Mar. 2022.
[27] Z. Shen, H. Wang, Y. Shen, Z. Qin, and F. Blaabjerg, "An improved stray capacitance model for inductors," *IEEE Trans. Power Electron.*, vol. 34, no. 11, pp. 11153–11170, Nov. 2019.
[28] H. Zhao et al., "Rethinking basic assumptions for modeling parasitic capacitance in inductors," *IEEE Trans. Power Electron.*, vol. 37, no. 7, pp. 8281–8289, Jul. 2022.
[29] H. Zhao et al., "A comparative study on parasitic capacitance in inductors with series or parallel windings," *IEEE Trans. Power Electron.*, vol. 37, no. 12, pp. 15140–15151, Dec. 2022.
[30] H. Zhao et al., "Physics-based modeling of parasitic capacitance in medium-voltage filter inductors," *IEEE Trans. Power Electron.*, vol. 36, no. 1, pp. 829–843, Jan. 2021.
[31] X. Liu, Y. Wang, J. Zhu, Y. Guo, G. Lei, and C. Liu, "Calculation of capacitance in high-frequency transformer windings," *IEEE Trans. Magn.*, vol. 52, no. 7, Jul. 2016, Art. no. 2003204.
[32] B. Cui, H. Shi, Q. Sun, X. Tang, L. Hong, and B. Zhao, "A novel analysis, design, and optimal methodology of high-frequency oscillation for dual active bridge converters with WBG switching devices and nanocrystalline transformer cores," *IEEE Trans. Power Electron.*, vol. 36, no. 7, pp. 7665–7678, Jul. 2021.
[33] C. C. Sekhar, C. Nagamani, G. Saravana Ilango, and S. Mageshwari, "Mitigation of high-frequency oscillation in a multiport DC-DC converter," in *Proc. IEEE Int. Conf. Power Electron., Drives Energy Syst.*, 2022, pp. 1–6.
[34] S. Wei and W. Wen, "High-frequency oscillation of the active-bridge-transformer-based DC/DC converter," *Energies*, vol. 15, no. 9, May 2022, Art. no. 3311.
[35] A. Cremasco, D. Rothmund, M. Curti, and E. A. Lomonova, "Voltage distribution in the windings of medium-frequency transformers operated with wide bandgap devices," *IEEE J. Emerg. Sel. Topics Power Electron.*, vol. 10, no. 4, pp. 3587–3602, Aug. 2022.
[36] R. Prieto, J. A. Cobos, O. Garcia, P. Alou, and J. Uceda, "Study of 3-D magnetic components by means of 'Double 2-D' methodology," *IEEE Trans. Ind. Electron.*, vol. 50, no. 1, pp. 183–192, Feb. 2003.
[37] J. Biela and J. W. Kolar, "Using transformer parasitics for resonant converters—A review of the calculation of the stray capacitance of transformers," *IEEE Trans. Ind. Appl.*, vol. 44, no. 1, pp. 223–233, Jan. 2008.
[38] R. P. Wojda and M. K. Kazimierczuk, "Winding resistance and power loss of inductors with litz and solid-round wires," *IEEE Trans. Ind. Appl.*, vol. 54, no. 4, pp. 3548–3557, Jul./Aug. 2018.
[39] F. G. Brockman, P. H. Dowling, and W. G. Steneck, "Dimensional effects resulting from a high dielectric constant found in a ferromagnetic ferrite," *Phys. Rev.*, vol. 77, no. 1, pp. 85–93, Jan. 1950.
[40] S. Takahashi, S. Ogasawara, M. Takemoto, K. Orikawa, and M. Tamate, "Experimental evaluation of the relationship between filter inductor impedances and dimensional resonances of MnZn ferrites," in *Proc. IEEE 4th Int. Future Energy Electron. Conf.*, 2019, pp. 1–8.
[41] B. Wunsch, T. Christen, S. Skibin, and V. Forsstrom, "Broadband circuit model of a ferrite core, including dimensional resonance, saturation, and hysteresis," *IEEE Trans. Magn.*, vol. 55, no. 7, Jul. 2019, Art. no. 7300605.
[42] H. Zhao, Y. Li, Q. Lin, and S. Wang, "The parasitic capacitance of magnetic components with ferrite cores due to time-varying electromagnetic (EM) field," in *Proc. IEEE Energy Convers. Congr. Expo.*, 2018, pp. 3534–3541.
[43] N. Hou and Y. W. Li, "Overview and comparison of modulation and control strategies for a nonresonant single-phase dual-active-bridge DC–DC converter," *IEEE Trans. Power Electron.*, vol. 35, no. 3, pp. 3148–3172, Mar. 2020.

Yueyin Wang was born in Liaoning, China, in 1996. He received the B.S. degree in electrical engineering and automation from the Shenyang Institute of Engineering, Liaoning, China, in 2018, and the M.S. degree in electrical engineering from the North China Electric Power University, Beijing, China, in 2021. He is currently working toward the Ph.D. degree in electrical engineering with the Southeast University, Nanjing, China.

His research interests include active gate driver technology, converter electromagnetic modeling, and high-frequency transformer.

Wu Chen (Senior Member, IEEE) was born in Jiangsu, China, in 1981. He received the B.S., M.S., and Ph.D. degrees in electrical engineering from the Nanjing University of Aeronautics and Astronautics, Nanjing, China, in 2003, 2006, and 2009, respectively.

From 2009 to 2010, he was a Senior Research Assistant with the Department of Electronic Engineering, City University of Hong Kong, Hong Kong. In 2010 and 2011, he was a Postdoctoral Researcher with Future Electric Energy Delivery and Management Systems Center, North Carolina State University, Raleigh. Since 2011, he has been an Associate Research Fellow with the School of Electrical Engineering, Southeast University, Nanjing, China, where he has been a Professor since 2016. His main research interests include soft-switching converters, power delivery, and power electronic system integration.

Dr. Chen is an Associate Editor for IEEE TRANSACTIONS ON INDUSTRIAL ELECTRONICS, *Journal of Power Electronics*, and *CPSS Transactions on Power Electronics and Applications*.

Zhan Shen (Member, IEEE) received the B.E. degree in electrical engineering and automation from the Nanjing University of Aeronautics and Astronautics, Nanjing, China, in 2013, the M.E. degree in electrical engineering from the Southeast University, Nanjing, China, in 2016, and the Ph.D. degree in energy technology from the Aalborg University, Aalborg, Denmark, in 2020.

He is currently an Associate Professor with the Southeast University, Nanjing, China. He was a Visiting Scholar with the RWTH Aachen University, Aachen, Germany, and with the Massachusetts Institute of Technology, Cambridge, MA, USA. He was with the ABB Corporate Research Center, Beijing, China, in 2016. His research interests include power electronic system integration, magnetic components, and artificial intelligence.

Xiao Yu was born in Sichuan province, China, in 1993. He received the B.S. degree in electrical engineering and automation and the Ph.D. degree in electrical engineering from Chongqing University, Chongqing, China, in 2015 and 2020, receptively.

In 2018 and 2019, he was a visiting scholar with the University of Warwick, U.K., in 2018. Since 2020, he has been an Assistant Research Fellow with the Electronic Institute, China Academy of Engineering Physics. His research interests include the reliability of power electronic equipment, the multiphysics modeling, and computation of power electronic equipment.

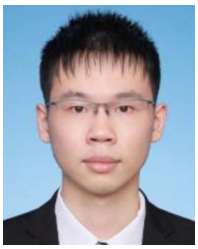

Xuhao Zhu was born in Nanjing, China, in 1998. He received the B.S. degree in communication engineering from Nanjign University of Post and Telecommunications, Nanjing, China, in 2020, the M.S. degree in electrical engineering in 2023 from Southeast University, Nanjing, China, where he is currently working toward the Ph.D. degree in electrical engineering.

His current research interest includes power electronics.

Haozhe Jin (Graduate Student Member, IEEE) was born in Zhejiang, China, in 1997. He received the B.S. degree in electrical engineering from the Southwest Jiaotong University, Chengdu, China, in 2019. He is currently working toward the Ph.D. degree in electrical engineering from the Southeast University, Nanjing, China.

His research interests include the dc transformer and soft switching dc–dc converter.

Siyi Luo (Graduate Student Member, IEEE) was born in Jiangxi, China, in 1996. He received the B.S. degree from East China Jiaotong University, Jiangxi, China, in 2018, and the M.S. degree from Shanghai Maritime University, Shanghai, China, in 2022, both in electrical engineering. He is currently working toward the Ph.D. degree in electrical engineering with the Southeast University, Nanjing, China.

His current research interests include power electronics, distributed generation, renewable energy systems, and grid forming control.

Zewei Hao was born in Inner Mongolia, China, in 1996. He received the B.S. and M.S. degrees in electrical engineering from Wuhan University, Wuhan, China, in 2019 and 2021, respectively. He is currently working toward the Ph.D. degree in electrical engineering with Southeast University, Nanjing, China.

Xin Li (Member, IEEE) received the B.S. and Ph.D. degrees in electrical engineering and automation from Nanjing University of Aeronautics and Astronautics, Nanjing, China, in 2012 and 2018, respectively.

In 2019, he was a Research Engineer with Huawei Technologies Co., Ltd., Shanghai, China. From 2020 to 2022, he was a Research Fellow with Nanyang Technological University, Singapore. Since 2022, has been an Associate Researcher with the School of Electrical Engineering, Southeast University, Nanjing, China. His current research interests include modeling, control and design of PWM converter, resonant converter, and wireless power transfer system.